

Beyond conventional migration: non-linear elastic subsalt imaging with transmissions and two-sided illumination

Matteo Ravasi,¹ Ivan Vasconcelos² and Andrew Curtis¹

¹*Grant Institute of Earth Science, School of Geosciences, The University of Edinburgh, Edinburgh EH9 3JW, United Kingdom.*

E-mail: M.Ravasi@sms.ed.ac.uk

²*Schlumberger Gould Research Centre, High Cross, Madingley Road, Cambridge CB3 0EL, United Kingdom*

Accepted 2014 May 20. Received 2014 May 19; in original form 2014 January 16

SUMMARY

Source–receiver interferometric imaging can be used to synthesize a subsurface acoustic or elastic image, consisting of a zero-time, zero-offset response (or Green’s function) between a colocated pseudo-source and pseudo-receiver placed at each point in the subsurface image. However, if the imaging process does not properly account for multiple reflections, and enclosing boundaries of sources and receivers are not available, the image shows artefacts, poorly illuminated areas and distorted image amplitudes. Here we demonstrate with numerical examples that two-sided non-linear imaging provides the best elastic pure-mode (*PP* and *SS*) and converted-mode (*PS*) images, having higher resolution and more uniform illumination than those obtained from both one-sided linear imaging and from other intermediate steps of imaging (e.g. non-linear one-sided, linear two-sided). We also propose practical approaches to construct the additional fields required by two-sided non-linear imaging without the need for a detailed velocity model and receivers (and/or sources) in the subsurface. Moreover, when conversions are used for imaging, ‘true-amplitude’ images (here true-amplitude means properly retrieving amplitudes that represent the zero-time, zero-offset elastic response) should theoretically vanish because neither *P*-to-*S* or *S*-to-*P* conversions arise at zero-time and zero-offset. Applying a correction procedure that accounts for the polarity reversal in *PS* (or *SP*) single-shot images helps with their structural interpretation but results in an unphysical estimate of the subsurface response and uninterpretable amplitudes. This suggests that there are advantages in exploiting pure-mode *SS* reflections/transmissions, in addition to converted waves only, because they require no polarity correction and the resulting image contains meaningful amplitudes that are proportional to the local shear-wave properties of the medium.

Key words: Interferometry; Controlled source seismology; Computational seismology; Wave scattering and diffraction; Wave propagation.

1 INTRODUCTION

An important goal of seismic processing is subsurface imaging (or migration) to estimate both the locations and amplitudes of discontinuities in subsurface properties. This is achieved by mapping or propagating the recorded wavefield back in to the subsurface to where reflections originate. A reflection involves the conversion of an incident wave into a scattered wave, commonly called the ‘source wavefield’ and ‘receiver wavefields’, respectively. The ‘imaging principle’ behind almost all imaging algorithms states that the reflector is located where source and receiver waves are non-vanishing at the same place and time because one creates the other (Claerbout 1971).

To apply the imaging principle requires two steps: first, numerical modelling of the source and receiver wavefields, where the former is obtained by forward modelling waves from the (known) source

and the latter is estimated by a so-called ‘wavefield extrapolation’ procedure that backpropagates the recorded data into the subsurface. Second, the zero-lag time correlation of these two fields (calculation of a so-called imaging condition) is evaluated at each subsurface (image) point. The result of the second step should ideally only be non-zero at points where the two wavefields are directly correlated, hence at subsurface discontinuities. In this paper, we analyse the improvements that are potentially offered by recent advances in imaging theory, particularly in complex elastic geologies.

The imaging problem was formulated using reciprocity integrals by Esmeroy & Oristaglio (1988) and Oristaglio (1989) in the context of Born imaging of primary reflection data. The double surface integration over boundaries of sources and receivers in such a formulation allowed a relationship to be derived between reciprocity-based imaging and a specific form of seismic interferometry, called source–receiver interferometry (SRI; Curtis 2009;

Curtis & Halliday 2010). Halliday & Curtis (2010) presented a source–receiver interferometric imaging framework where the imaging condition and wavefield extrapolation steps are expressed explicitly in terms of double integrals over source and receiver boundaries by using the scattering reciprocity theorems of Vasconcelos *et al.* (2009).

SRI integrals are exact and fully non-linear, removing the single-scattering assumption of Oristaglio (1989); however, they rely on the explicit evaluation of volume integrals of scattered fields to account for multiply-scattered waves, which are computationally too expensive for current seismic data and computing capabilities. Vasconcelos (2013) uses a modification of these reciprocity-based integrals where the volume integrals are replaced by surface integrals containing interactions of scattered fields with themselves, by invoking power conservation via the full-waveform version of the Generalized Optical Theorem (Fleury *et al.* 2010; Douma *et al.* 2011; Fleury & Vasconcelos 2012). Incorporating non-linear multiple-scattering effects in the imaging process (and using fully enclosing boundaries of sources and receivers) reduces imaging artefacts, improves illumination and preserves amplitudes as shown by Fleury & Vasconcelos (2012) and Ravasi & Curtis (2013a).

Another insight derives from the connection between SRI and source–receiver imaging. On the one hand, SRI synthesizes unmeasured wavefield responses (or band-limited Green’s functions) between a real source to a real receiver, using only energy recorded at a surrounding boundary of receivers and from a surrounding boundary of sources. On the other hand, source–receiver imaging generates fully non-linear (‘true-amplitude’) subsurface images whose amplitudes represent the zero-time, zero-offset scattered wave response between a colocated pseudo-source and pseudo-receiver at each image point within the subsurface (Vasconcelos 2008; Vasconcelos *et al.* 2010). This physical interpretation of an image as a scattered wavefield leads to various additional interpretative possibilities: for example, the wavefield can be observed and analysed at non-zero times and offsets, resulting in so-called extended images (e.g. Vasconcelos *et al.* 2010).

The availability of only a reference estimate of the background velocity model at the start of the imaging stage means that most imaging algorithms rely on a linear, single-scattering assumption in which all wavefields used for imaging must first have all multiples removed (Claerbout 1971; Oristaglio 1989; Biondi 2006). Such methods fail to handle complex scattering effects and therefore do not produce correct amplitudes of reflecting heterogeneities. To overcome this limitation, the full wavefield propagating from any point in the subsurface to the surface receiver array (including all waves that bounce multiple times between interfaces before reaching the acquisition surface) must be determined accurately in order to back-project the recorded multiple reflections/diffractions that travel from this subsurface point to the recording surface. Similarly, an estimate of the full wavefield from the source array to any subsurface point will allow the proper imaging of waves that bounce multiple times in their path from the source to the subsurface point. Estimating these wavefields appears to require a detailed model of subsurface reflectivity heterogeneities to be known in advance of imaging (which is in general unlikely).

However, alternative approaches have recently been introduced to estimate these wavefields in acoustic media: Fleury (2013) adopts an image-based approach, while Broggin *et al.* (2012) and Wapenaar *et al.* (2012, 2013) propose an almost purely data-driven approach called wave field ‘autofocusing’ for retrieving full acoustic Green’s function responses from a virtual source in the subsurface (i.e. at each image point) towards the recording array. In the former

method, the linear image is used to create a (first-order) estimate of the perturbation to the background model. Unfortunately, errors in estimating small-scale features in the model, both in terms of their spatial locations and magnitudes, turn directly into dynamic and kinematic inaccuracies of the full propagators modelled in this bootstrapped stratigraphic model. The latter method does not require the structural reflectors to be known in detail in advance of non-linear imaging: to estimate the full propagating Green’s functions it requires only reflection data at the surface and an estimate of the direct arrival propagating between the virtual source location and the acquisition surface. These estimated fields are less affected by kinematic errors than those obtained by the image-based approach, however an accurate estimate of the amplitude of the direct arrival and wide-offset reflection data are necessary to achieve dynamically correct fields. Finally, note that both methods can be used with reference models that contain sharp discontinuities from interpreted salt bodies and other converting boundaries (e.g. at the seabed). By henceforth assuming that the availability of a good estimate of such full wavefields (containing also the correct internal multiples) is granted, non-linear imaging can be applied also when initial knowledge of the medium is limited to a reference (smooth) velocity model.

The lack of enclosing boundaries represents another challenge to applying source–receiver imaging (or any migration method) in practice: the limitation in source and receiver aperture is known to cause image distortions that can be understood as spatially varying, directionally dependent local blurring (Lecomte 2008). van der Neut *et al.* (2013) presented a novel method that transforms conventional surface seismic data (sources and receiver at the surface) into data with sources and receivers above and below a selected target zone, by inverting a series of multidimensional interferometric equations of convolution- and correlation-type. The creation of a virtual acquisition geometry at a desired depth level can therefore upgrade the seismic imaging from the conventional one-sided illumination case to the two-sided illumination case, where transmissions can be used along with under-side reflections for a more uniform illumination of the target of interest.

When source–receiver imaging is formulated in elastic media (Ravasi & Curtis 2013b), the tensorial nature of the elastic wave equation leads to a range of alternative imaging conditions and definitions of what a true-amplitude elastic image can be. For example, we may construct an image whose amplitudes are the zero-offset, zero-time particle velocity field due to an external volume force pseudo-source, or are the compressional-wave (potential) field due to a shear-wave pseudo-source. Ravasi & Curtis (2013a) have shown that when potential fields (or equivalently *P*- and *S*-wave fields in isotropic media) are chosen, the true-amplitude *PS* image (the image describing the local interactions between incident *P* waves and emerging *S* waves) should completely vanish (by destructive interference of images from the various sources and receivers), since *P* to *S* conversions cannot arise at zero-time in zero-offset experiments.

The latter observation leads to two different possible approaches to *S*-wave imaging. When shear energy is used for ‘structural’ imaging—identification of structures in the subsurface from the images but without the need for meaningfully interpretable amplitudes of the images—then either *S*-to-*S* reflections/transmissions or *P*-to-*S* (and *S*-to-*P*) conversions can be used. When *S*-to-*S* waves are used, shear wave energy must reach each image point not only from the receiver wavefield (as is also the case for *PS* imaging) but also from the source wavefield. If the physical source does not generate *S*-wave energy such as in marine seismics, linear *S*-to-*S* imaging requires at least one (interpreted) hard boundary in the initial

where G and Φ are the source and receiver wavefields, respectively. ρ is the density and c_P is the P -wave velocity at the boundary of sources ∂V_S (both assumed constant), ω is the angular frequency and $*$ represents complex conjugation in the frequency domain (i.e. time-reversal in the time domain). In theory, it is important that the boundary ∂V_S fully encloses the imaging object in order to correctly recover the amplitudes of scattered fields. However, only limited-aperture, truncated source arrays are usually available in practice ($\partial V_{S,top}$ —solid black line in Fig. 1). Note that the assumption of ocean-bottom acquisition appears in the Φ terms where the fields are either P - or S -wave potentials in the subsurface, due only to P -source (pure pressure) excitation functions.

In eq. (3) the first integral performs the cross-correlation between the reference source wavefield (i.e. that computed in the reference model) and the receiver-side scattered wavefield. The second integral in eq. (3) constitutes the non-linear correction to the imaging condition (Fleury & Vasconcelos 2012; Ravasi & Curtis 2013b), which accounts for source-side internal multiples (i.e. internal multiples occurring between the physical source \mathbf{x}_S and the pseudo-receiver \mathbf{x}) through the scattered source wavefield.

The exact expressions for reconstructing the receiver-side wavefields in eq. (3) are

$$\begin{aligned} \Phi_M^S(\mathbf{x}, \mathbf{x}_S) = & \int_{\partial V_R} \left[p^S(\mathbf{x}_R, \mathbf{x}_S) G_{(M,z)}^{0(\phi,f)*}(\mathbf{x}, \mathbf{x}_R) \right. \\ & \left. - v_z^S(\mathbf{x}_R, \mathbf{x}_S) G_{(M,zz)}^{0(\phi,h)*}(\mathbf{x}, \mathbf{x}_R) \right] d\mathbf{x}_R \\ & + \int_{\partial V_R} \left[p^t(\mathbf{x}_R, \mathbf{x}_S) G_{(M,z)}^{S(\phi,f)*}(\mathbf{x}, \mathbf{x}_R) \right. \\ & \left. - v_z^t(\mathbf{x}_R, \mathbf{x}_S) G_{(M,zz)}^{S(\phi,h)*}(\mathbf{x}, \mathbf{x}_R) \right] d\mathbf{x}_R, \end{aligned} \quad (4)$$

and

$$\begin{aligned} \Phi_M^t(\mathbf{x}, \mathbf{x}_S) = & \int_{\partial V_R} \left[p^t(\mathbf{x}_R, \mathbf{x}_S) G_{(M,z)}^{t(\phi,f)*}(\mathbf{x}, \mathbf{x}_R) \right. \\ & \left. - v_z^t(\mathbf{x}_R, \mathbf{x}_S) G_{(M,zz)}^{t(\phi,h)*}(\mathbf{x}, \mathbf{x}_R) \right] d\mathbf{x}_R, \end{aligned} \quad (5)$$

where p and v_z are the pressure and vertical particle velocity recordings, respectively, and eqs (4) and (5) also come from representation theorems (Wapenaar & Fokkema 2006; Ravasi & Curtis 2013a). Here the G terms represent the receiver-side propagators, superscripts f and h are used to define external volume force sources and external deformation rate sources respectively, and subscripts z/zz identify the z th/ zz th component of these sources when z is vertically downwards. Similarly to the source boundary in the imaging condition, the receiver boundary ∂V_R should enclose the imaging object to achieve ‘true-amplitude’ imaging. Finally note that, as source-side scattered propagators G^S can be computed by subtracting the reference propagators computed in the background model from the full propagators computed in the exact model, receiver-side scattered propagators Φ^S can be equivalently obtained by backpropagating the required data both in the background and exact model and subtract the two extrapolated wavefields.

The first integral in eq. (4) is linear in the relation between data and the extrapolation model: reference propagators are used to backpropagate the recorded, scattered wavefield into the subsurface. By contrast the second integral in eq. (4) and that in eq. (5) are non-linear in the extrapolation model, because (full) recorded data are extrapolated through scattered and total propagators both of which

include receiver-side internal multiples. Thus the latter terms include scattered recorded data interacting with scattered wave propagators resulting in a non-linear relation between the image and the (*a priori* unknown) scattering perturbations. Note that if the scattered field in the first integral of eq. (3) is obtained by means of linear wavefield extrapolation, this integral becomes equivalent to a conventional cross-correlation imaging condition (e.g. Chang & McMechan 1994; Yan & Sava 2008), otherwise when non-linear wavefield extrapolation is carried out, the imaging condition also accounts for the receiver-side internal multiples (i.e. internal multiples occurring between the physical receiver \mathbf{x}_R and the pseudo-source image point \mathbf{x}).

The image given by the combination of eqs (3)–(5) is thus fully non-linear on both the acquired data and the subsurface model. It accurately focuses the energy from multiple scattering interactions along with primary scattering, provided that scattered wave propagators are available. We therefore refer to this imaging procedure as non-linear elastic reverse-time migration (NLERTM). In the context of traditional elastic reverse-time migration (ERTM) where only primaries are used to map unknown discontinuities in the subsurface via knowledge of a reference model, eqs (3) and (4) can be simplified under a Born approximation (i.e. single scattering assumption) and combined together, to give a linear image

$$\begin{aligned} I_{MN}^l(\mathbf{x}) = & \frac{2}{\rho c_P} \int \left(\int_{\partial V_S} G_{(N,P)}^{0(\Phi,\Phi)*}(\mathbf{x}, \mathbf{x}_S) \right. \\ & \times \int_{\partial V_R} \left(\tilde{p}^S(\mathbf{x}_R, \mathbf{x}_S) G_{(M,z)}^{0(\phi,f)*}(\mathbf{x}, \mathbf{x}_R) \right. \\ & \left. \left. - \tilde{v}_z^S(\mathbf{x}_R, \mathbf{x}_S) G_{(M,zz)}^{0(\phi,h)*}(\mathbf{x}, \mathbf{x}_R) \right) d\mathbf{x}_R d\mathbf{x}_S \right) d\omega, \end{aligned} \quad (6)$$

where \tilde{p}^S and \tilde{v}_z^S indicate a dependence on Born data that approximate the full recorded data (p^S and v_z^S) by neglecting multiple scattering (Wapenaar *et al.* 2010). Finally, we define one-sided illumination when $\partial V_R = \partial V_{R,top}$ and $\partial V_S = \partial V_{S,top}$, while two-sided illumination is given by $\partial V_R = \partial V_{R,top} \cup \partial V_{R,bot}$ and $\partial V_S = \partial V_{S,top} \cup \partial V_{S,bot}$ (see Fig. 1).

3 NUMERICAL EXAMPLE

We now compare linear and non-linear images in a complex medium. We present a numerical example where P -to- P , P -to- S and S -to- S images are computed using a modified version of the synthetic model Pluto 1.5 released by the SMAART JV consortium (Stoughton *et al.* 2001). Our model is created by flattening the seabed at a depth of $z_{seabed,1} = 760$ m and since we want to test two-sided imaging we also add a second water layer at the bottom of the model ($z_{seabed,2} = 7600$ m). Thus we can model pure P -wave sources also along the boundary below the imaging target (otherwise additional S -wave sources would be required in the lowermost solid media by the imaging condition in eq. 3). Fig. 2(a) shows the true P -wave model and Fig. 2(b) shows the reference model used for conventional (linear) imaging. The latter is obtained by smoothing the model in Fig. 2(a) while keeping sharp boundaries at the fluid-solid interfaces and at the edges of the salt bodies. Fig. 2(c) displays the difference between true and reference model, which represents the unknown perturbation that we would like to image. The S -wave velocity model is a scaled version of the P -wave velocity with a linearly depth-variant ratio ranging from 0.5 at $z_{seabed,1}$ to 0.7 at $z_{seabed,2}$. The ratio is, however, kept constant inside the two

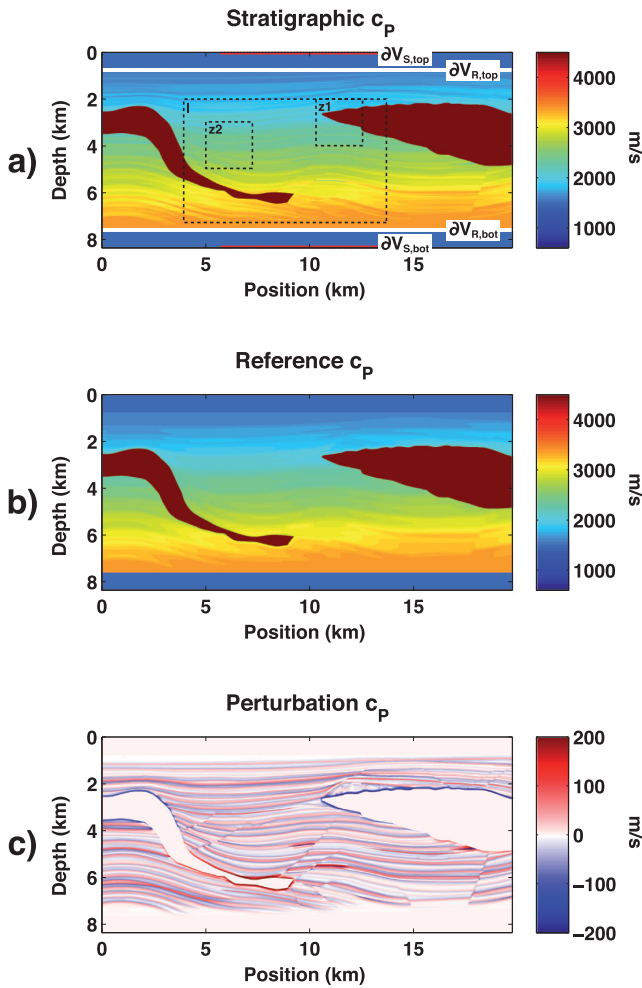


Figure 2. Pluto models. Stratigraphic P -wave velocity model is shown in (a) along with the shot locations (along red lines) and receiver geometry (white lines). The elastic images are computed inside the windowed area 'I', and areas 'z1' and 'z2' represent a portion of one of the salt bodies and a layered structure around a fault, respectively. The P -wave migration velocity model shown in (b) is a smoothed version of the true model but with sharp boundaries around the salts and for upper and lower seabeds, while (c) shows the true P -wave velocity perturbation [the difference between (a) and (b)].

salt bodies ($V_S/V_P = 0.55$). Finally, the density is obtained from the P -wave velocity through the well-known Gardner's relationship $\rho = 0.23 V_P^{0.25}$ (Gardner *et al.* 1974).

Two truncated, limited-aperture boundaries of 51 monopole P -wave sources at depths of $z_{S,1} = 40$ m and $z_{S,2} = 8320$ m with horizontal spacing of $\Delta x_S = 152$ m are used to model the synthetic data together with two boundaries of multicomponent receivers (white lines in Fig. 2(a)) placed along the upper and lower seabeds throughout the extension of the model with horizontal spacing of $\Delta x_R = 7.6$ m. The modelling is carried out using a Ricker wavelet pulse with 15 Hz peak frequency and absorbing boundaries (i.e. without a free-surface), otherwise further dipole P -wave sources would be required for a proper handling of in- and out-going waves at the source boundary ∂V_S (van Manen *et al.* 2007; Vasconcelos 2013; Vasmel *et al.* 2013).

We carry out six different imaging experiments which are represented schematically in Fig. 3, where different combinations of sources and receivers, and linear and non-linear terms are used.

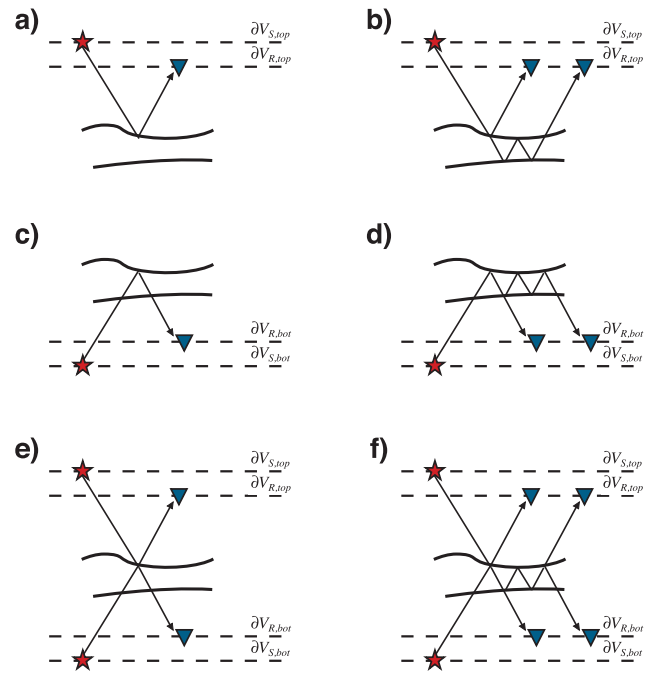


Figure 3. Schematic representation of the six different imaging experiments. (a) One-sided (top) elastic reverse-time migration (ERTM – which is linear), (b) one-sided (top) non-linear elastic reverse-time migration (i.e. NLERTM), (c) one-sided (bottom) ERTM, (d) one-sided (bottom) NLERTM, (e) two-sided ERTM, (f) two-sided NLERTM. Black rays identify the type of events accounted for in each of the experiments: one-sided imaging uses reflections only, whereas two-sided imaging also uses transmissions to improve the imaging result. Moreover, linear imaging only accounts for focusing of the primary reflections and transmissions while non-linear imaging handles also multiple reflections and transmissions with multiple reflections.

Elastic images of pure-mode reflections/transmissions (P -to- P and S -to- S) and conversions (P -to- S) are compared in terms of resolution, illumination and presence of cross-talk noise. We devote special attention to the areas just above and below one of the salt bodies where issues of illumination (below) and cross-talk (above) are usually severe. The quality of reconstruction of the complex stratigraphy around one of the faults in the subsurface will also be studied for the different imaging results.

3.1 PP images

Fig. 4 shows PP image obtained by means of one-sided (top panel) reflection ERTM (i.e. conventional Born elastic reverse-time migration) juxtaposed with that of one-sided (top panel) reflection NLERTM. The improvement arising from the additional focusing of multiple-scattered energy (i.e. internal multiples) at any image point is remarkable. Interfaces are more clearly defined at all depths, there is a general increase in spatial resolution of the image structure, and areas that are poorly illuminated by single-scattering events are now better resolved. The artefacts affecting the top of the salt body on the right are significantly suppressed, and the non-linear image (Fig. 4b) reveals the complex structure showing the power of migrating multiples together with primaries.

Next, we study the value of having a second boundary of sources and receivers at the bottom of the model, but we first assume that top and bottom boundaries are used in two separate reflection imaging experiments. As a general remark, one-sided (bottom panel)

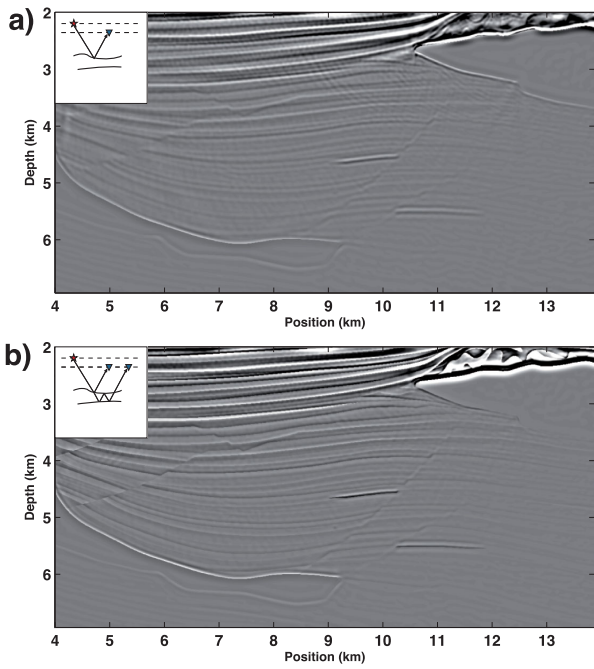


Figure 4. *PP* images obtained by means of (a) linear and (b) non-linear source–receiver, elastic reverse-time imaging using sources and receivers only above the imaging target (i.e. $\partial V_{S,top}$ and $\partial V_{R,top}$ in Fig. 2).

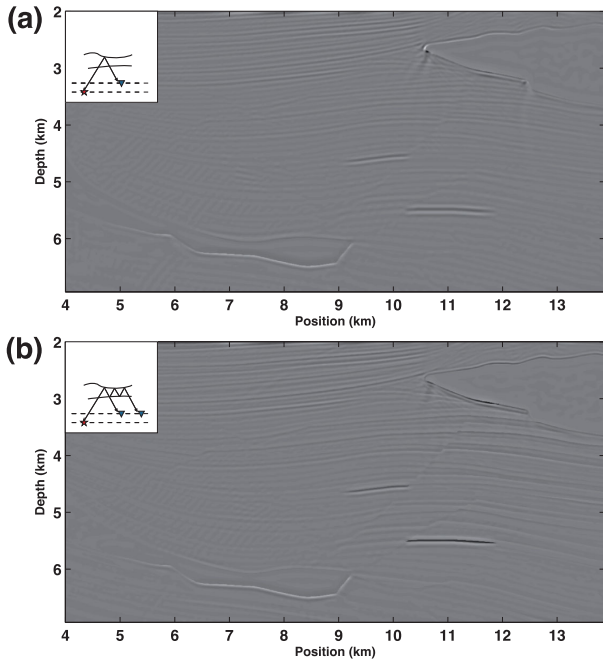


Figure 5. *PP* images obtained by means of (a) linear and (b) non-linear source–receiver, elastic reverse-time imaging using sources and receivers only below the imaging target (i.e. $\partial V_{S,bot}$ and $\partial V_{R,bot}$ in Fig. 2).

reflection ERTM (Fig. 5a) and NLERTM (Fig. 5b) images have smaller amplitudes¹ compared to images from top sources and receivers because of the higher impedance contrast at the bottom seabed. Illumination of the imaging target from different directions helps to construct a more isotropically illuminated final image of

¹Note: all images are displayed in the same range of amplitudes.

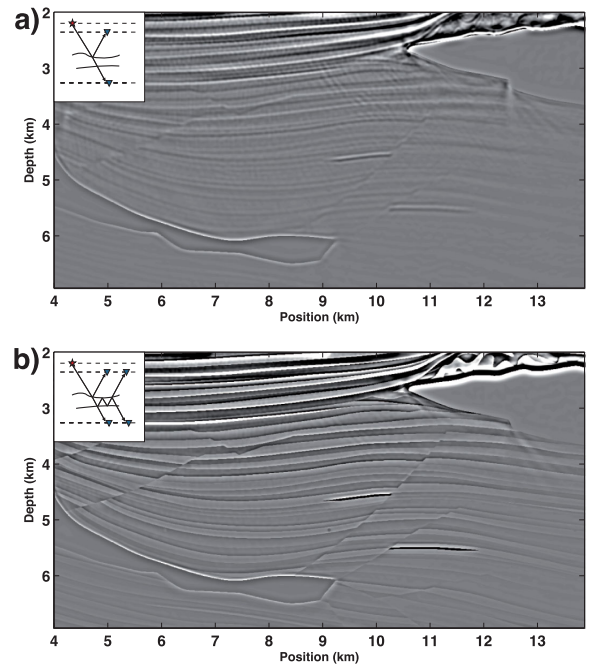


Figure 6. *PP* images obtained by means of (a) linear and (b) non-linear source–receiver, elastic reverse-time imaging using sources above (i.e. $\partial V_{S,top}$ in Fig. 2) and receivers both above and below the imaging target (i.e. $\partial V_R = \partial V_{R,top} \cup \partial V_{R,bot}$).

the subsurface, and to compensate for cross-talk artefacts that arise in the elastic images when only data from top sources and receivers are migrated. Reflection events (both primaries and multiples) generated by sources placed within the medium below the salt bodies, for example, give rise to a better image of the layered structure below the salt on the right (Fig. 5) compared to that of reflections from the top (Fig. 4).

Reflections and transmissions are finally combined together by the simultaneous use of top and bottom source and receiver boundaries. Note that when we use the term ‘transmissions’ we refer to globally transmitted waves that are emitted on one side of the imaging target and recorded on the opposite side. In Fig. 6 we show the advantage of recording data at two different depth levels (top and bottom panels) when only top sources are available, while in Fig. 7 we display images that are effectively computed from a full source–receiver two-sided illumination as depicted in Figs 3(e) and (f). Transmissions to contain useful additional information that is responsible for more accurate imaging below salt bodies (high-impedance obstructions) as is clearly visible by comparing, for example, Figs 6(a) with 4(a) and Figs 6(b) with 4(b). Two-sided sources, on the other hand, add contributions throughout the imaging target that equalize the amplitudes in the final image (Fig. 7b). The overall improvement provided by transmitted waves in imaging might come from the difference between the (series of) transmission and the (series of) reflection coefficients, one being high energy when the other is low energy and vice versa. Specifically for the deeper reflectors, transmitted waves have travelled a shorter path (from top to bottom) than reflections (from top to reflector to top again), thus losing less energy because of geometric spreading and scattering. Finally, the improvements in reflectors consistency below the salt bodies may occur because waves recorded at the bottom receiver array include a ‘fan’ of waves emitted by sources laterally far from each salt body, and hence which have travelled without interacting with strong impedance contrast of the salt bodies.

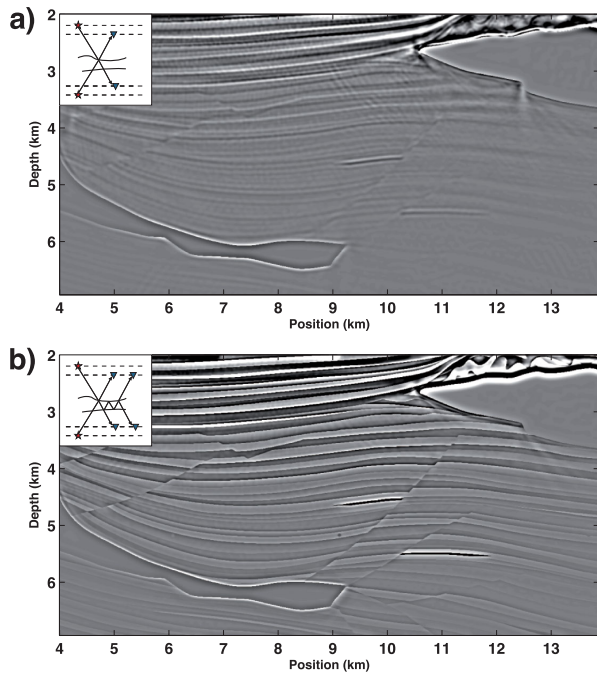


Figure 7. *PP* images obtained by means of (a) linear and (b) non-linear source-receiver, elastic reverse-time imaging using sources and receivers both above and below the imaging target (i.e. $\partial V_S = \partial V_{S, top} \cup \partial V_{S, bot}$ and $\partial V_R = \partial V_{R, top} \cup \partial V_{R, bot}$ in Fig. 2).

In Figs 8 and 9 close-ups of the portion of the images around the salt body on the right and one of the faults in the model are shown for the different imaging experiments discussed above. Again note the increase in spatial resolution and illumination arising from proper handling of multiple reflections. Moreover, adding sources and receivers at a given depth level results in images with more uniform amplitudes (Figs 8f and 9f).

3.2 Shear-wave (*SS* and *PS*) images

Elastic data like those recorded by ocean-bottom acquisition systems offer the possibility to image using *S*-wave energy, either (*S*-to-*S*) purely reflected or (*P*-to-*S* or *S*-to-*P*) converted energy. The different behaviour of shear waves compared to compressional waves has, however, long presented challenges in the practice of seismic imaging. Note that in our formulation of the imaging problem, *S*-to-*S* imaging can be performed without *S*-wave sources. Since converted *S*-wave energy reaches every point in the image and is scattered by heterogeneities, *S*-to-*S* images are constructed by evaluating $I_{SS}(\mathbf{x})$ in eq. (2). Similarly, *P*-to-*S* images are obtained by evaluating $I_{PS}(\mathbf{x})$.

Here, we first use shear-wave energy for ‘structural’ imaging, with the primary objective of reconstructing the structure of reflectors/diffractors but not necessarily attempting to retrieve the correct dynamics of $G^S(\mathbf{x}, \mathbf{x}, t = 0)$ in the imaging condition. *PS* and *SS* images are compared using linear and non-linear terms, and one- and two-sided imaging for our synthetic example. The first image displayed in Fig. 10 is the result of *P*-to-*S* one-sided (top) reflection ERTM when stacking over shots, without the application of any polarity correction procedure. Apart from the spurious energy just above the salt body on the right resulting from the interaction of strong converted waves in the source and receiver wavefields, we

barely see any interfaces because of the destructive interference of single-shot images, and this effect becomes more and more apparent as we stack more and more shots.

In Fig. 11(a) the same single-shot images are stacked together after correcting for the polarity change by simply multiplying by -1 the images on one side of each shot position while keeping the other side unchanged. Although the quality of the *P*-to-*S* ERTM image is not comparable to that obtained from a *P*-to-*P* imaging condition, some of the shallow interfaces and the two reservoirs are still resolved. Figs 11(b) to (f) display converted-wave images obtained from the other imaging experiments in Fig. 3 after applying the polarity correction procedure. While linear (and non-linear) reflections from the bottom acquisition geometry contribute in the same way as those in *P*-to-*P* imaging by basically enhancing the quality of the image in areas poorly illuminated by primaries (e.g. below the salt bodies), *P*-to-*S* transmissions show a remarkable lower frequency content (see Figs 11e and f) compared to their compressional-wave counterparts (Figs 7a and b) and converted-wave reflections (Figs 11a–d). While this behaviour of non-linear *PS* images is still under study, at this point we believe that the low frequency content in these images is largely non-physical in nature, and is due to the departure from the scattered field definition of the image when the polarity correction is applied.

Similarly to *P*-to-*P* and *P*-to-*S* imaging, in Fig. 12 we display pure shear-wave images obtained from the different imaging experiments in Fig. 3. Note that in marine ocean-bottom acquisition systems sources cannot directly generate shear waves because they are placed inside the water layer. *S*-to-*S* conventional (linear) imaging thus requires the additional, accurate knowledge of one or more sharp boundaries (e.g. fluid-solid interfaces or the edge of the salt bodies) for the generation of *S*-wave energy in the source wavefield. By contrast, all interfaces present in the stratigraphic model are generators of shear waves in non-linear imaging since the full (and scattered) propagators are directly modelled in the exact model. Both recorded shear wave energy and the same interfaces produce *S*-wave energy in the receiver wavefield for all six imaging configurations.

Pure-mode shear wave imaging does not require any additional processing step to account for positive and negative reflection coefficients because the polarity of shear reflections/transmissions is such that the procedure of stacking over shots has a naturally constructive behaviour. It is also worth noting that, although the quality of *S*-to-*S* images (Fig. 12) is generally higher than that of polarity-corrected *P*-to-*S* images (Fig. 11), the interaction between shear wave energy in the source and receiver wavefield produces prominent artefacts at strong diffractors such as at the edges of the salt bodies. Although this needs to be studied in more detail, these artefacts are likely caused by the fact that *SS* images rely entirely on the conversion of *P*- to *S*-transmission at the seafloor. While *P*-to-*P* transmission occurs over the entire range of incidence angles, *P*-to-*S* transmission is therefore restricted to a subset of incident angles limited by the critical angle (which is controlled by the ratio of *P*-to-*S* velocities at the seafloor). As a result, a pure mode *S*-wave image in this case can be considerably angle-limited in terms of image coverage; this in turn generates focusing artefacts of the kind observed in our *SS* images. Gaiser & Vasconcelos (2010) observed this angle-dependent restriction in reconstructing pure-mode shear-waves in interferometry from field OBC data. Their analysis applies directly to our imaging scheme, which is a subsurface-domain interferometric reconstruction of pure-mode *S* waves. An important consequence of this dependence on seafloor *P*-to-*S* velocity ratio is that, even in acquisition scenarios with very wide aperture source

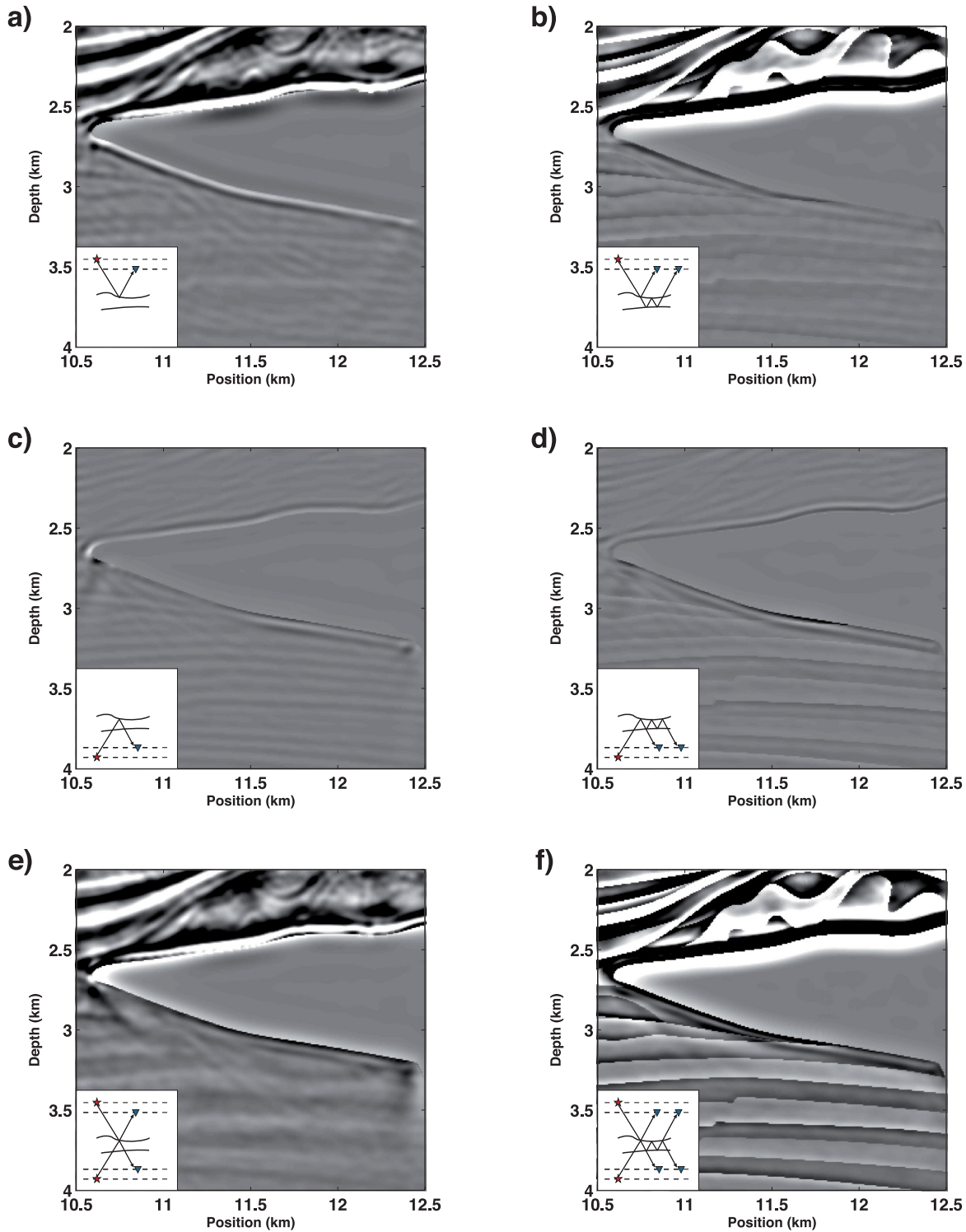


Figure 8. Salt body *PP* images for the six different imaging experiments depicted in Fig. 3, for region z1 in Fig. 2(a). Figs 8(a) and (b) are close-ups of Figs 4(a) and (b), Figs 8(c) and (d) are close-ups of Figs 5(a) and (b) and Figs 8(e) and (f) are close-ups of Figs 7(a) and (b).

and receiver arrays, the pure-mode *S*-wave images from ocean bottom data will always be more limited in aperture compared to their *P*-wave counterparts, and their subsurface illumination will largely depend on the seafloor properties.

We would like to use shear-wave energy also for true-amplitude imaging in order to extract meaningful amplitudes

that carry information about *S*-wave velocities. Ravasi & Curtis (2013b) have recently showed that in the ideal acquisition and imaging scenario (i.e. if the imaging process properly accounts for multiple scattering, and enclosing boundaries are used) the true-amplitude *PS* image vanishes. Our converted-wave image arising from two-sided NLRTM without polarity

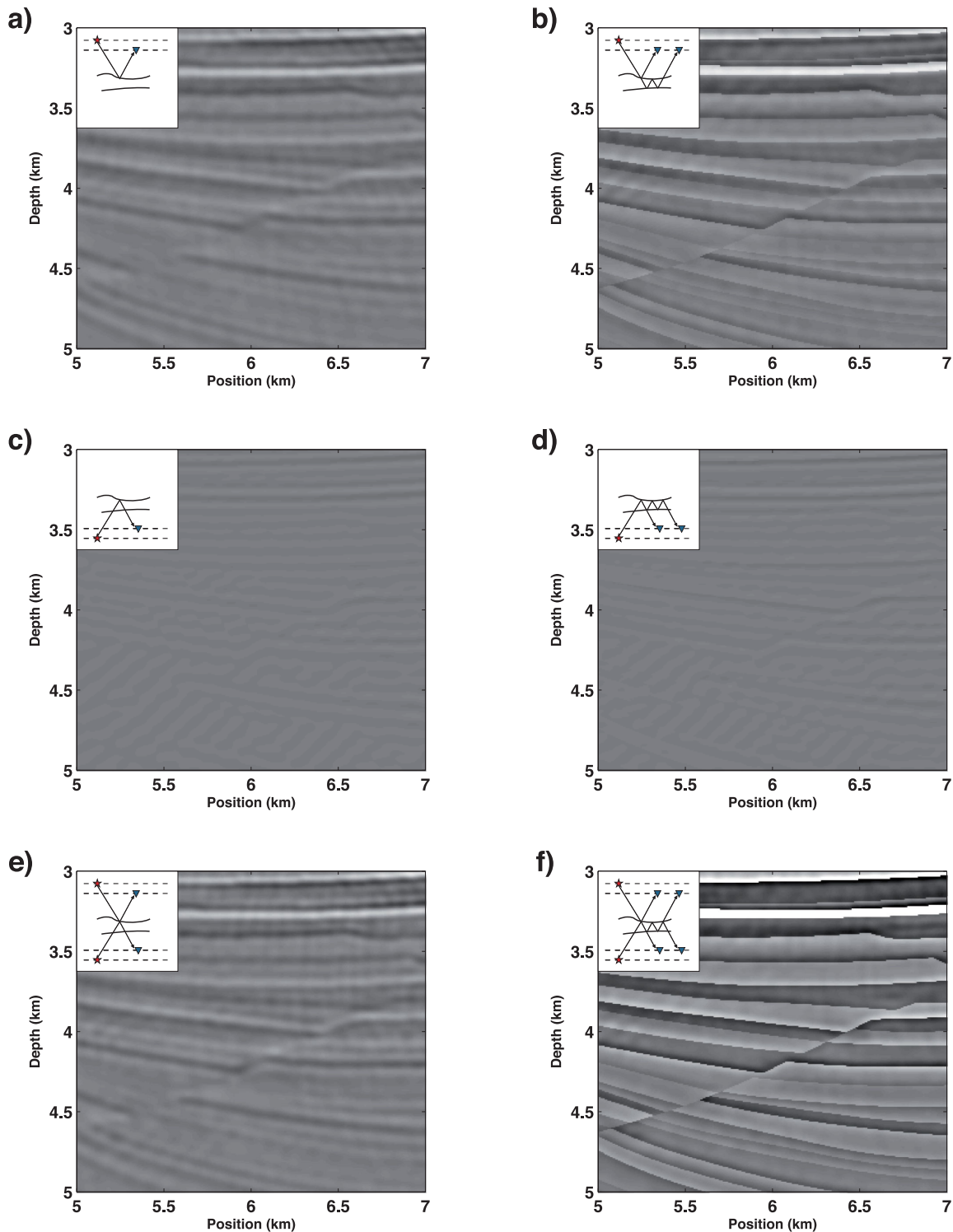


Figure 9. Fault *PP* images for the six different imaging experiments depicted in Fig. 3, for region z2 in Fig. 2(a). Figs 9(a) and (b) are close-ups of Figs 4(a) and (b), Figs 9(c) and (d) are close-ups of Figs 5(a) and (b) and Figs 9(e) and (f) are close-ups of Figs 7(a) and (b).

correction (Fig. 13) does however show residual non-physical energy which is not properly cancelled. This is the effect of using incomplete boundaries of receivers and, especially, sources (there are missing sources and receivers on either side of the cross-section), although the target is illuminated from both above and below.

To overcome the issues arising from limited-aperture source and receiver acquisition surfaces and check that this reasoning is correct, a local seismic experiment is carried out considering only a portion of the Pluto model embedded in an otherwise homogeneous medium (Fig. 14a) using a full, enclosing boundary of sources. The imaging condition in eq. (3) is evaluated by direct

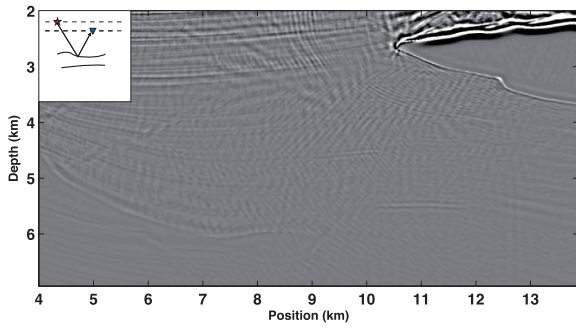


Figure 10. PS linear ERTM image using sources and receivers above the imaging target without correcting for converted shear wave polarity reversal.

modelling of the required reference and full wavefields (analogously to Fleury & Vasconcelos 2012) and the resulting image is displayed in Fig. 14(d), as a result of summing of the purely linear terms in the first integral of eq. (3) (Fig. 14b) and purely non-linear terms in the second integral of eq. (3) (Fig. 14c). The linear and non-linear contributions match and cancel out. As expected from the theory, the PS image (Fig. 14d) is indeed close to zero everywhere.

4 DISCUSSION

Multiple reflections are usually treated as ‘noise’ in seismic data processing, which should be estimated and removed prior imaging (Verschuur *et al.* 1992; Berkhout & Verschuur 1997; Weglein *et al.* 1997; Jakubowicz 1998; Amundsen 2001; ten Kroode 2002). Residual energy from multiples, which is not perfectly removed by the multiple attenuation algorithm, generates imaging artefacts in standard reverse-time migration arising from cross-talk of events in the source and receiver wavefields that are not physically related (e.g. a primary in the source wavefield interacting with a multiple in the receiver wavefield). This point of view is now moot, as geophysicists now consider multiples to be a source of useful information and attempt to use them in the imaging process (e.g. Muijs *et al.* 2007; Vasconcelos *et al.* 2008; Berkhout & Verschuur 2011; Liu *et al.* 2011; Davydenko & Verschuur 2012; Zhang & Schuster 2014).

Limited aperture boundaries of sources and receivers also present a limitation to the practice of seismic imaging. One way to alleviate the illumination problem is to solve the migration problem in a least-squares sense (using least-squares migration—see Nemeth *et al.* 1999). Alternatively, given that the image distortions can be thought of as local blurring filters (also called point-spread functions), an estimate of these blurring filters can be obtained by means of migration–demigration (Lecomte 2008; Gherasim *et al.* 2010;

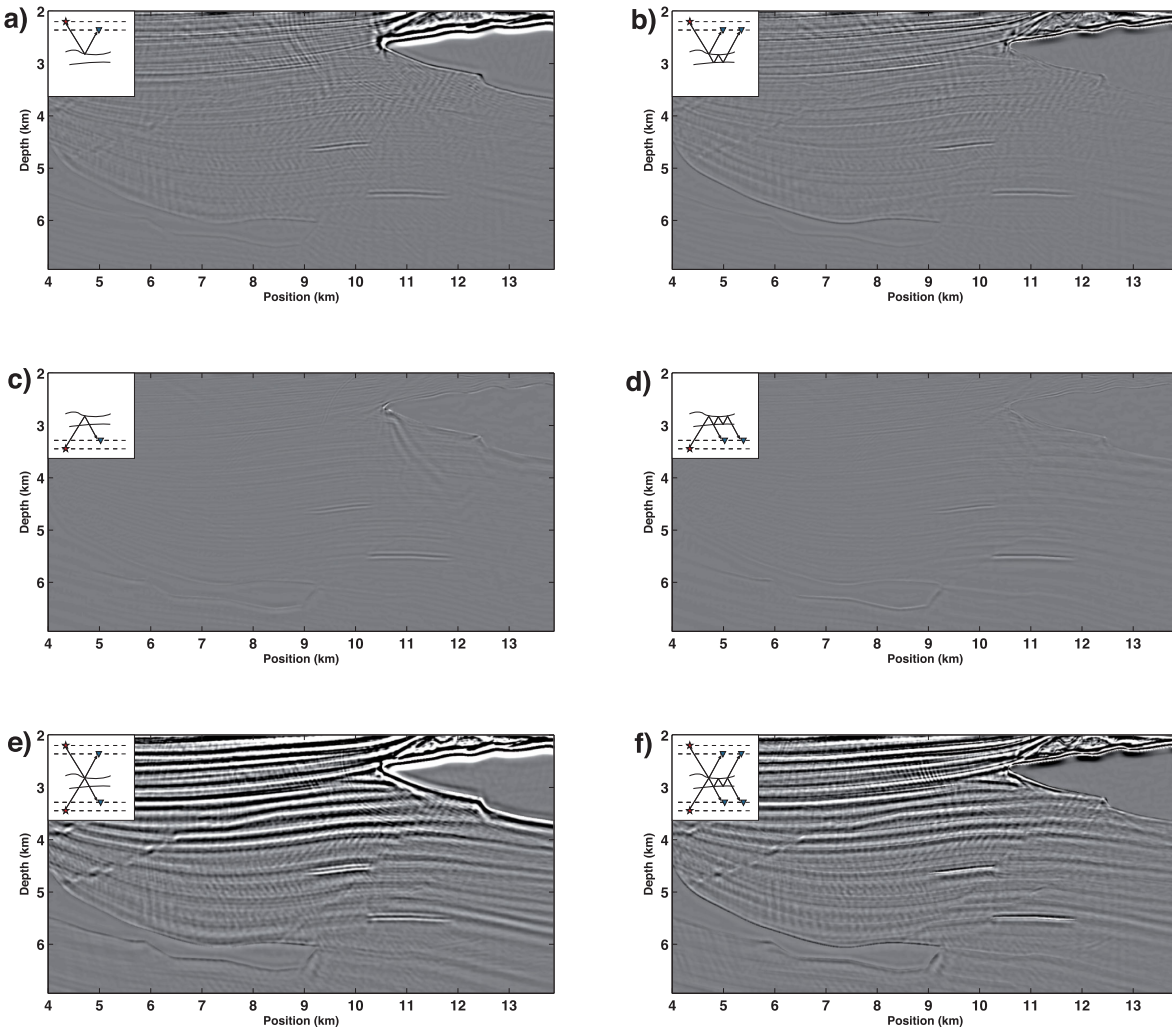


Figure 11. PS images obtained by applying a correction for polarity reversal for the six different imaging experiments depicted in Fig. 3.

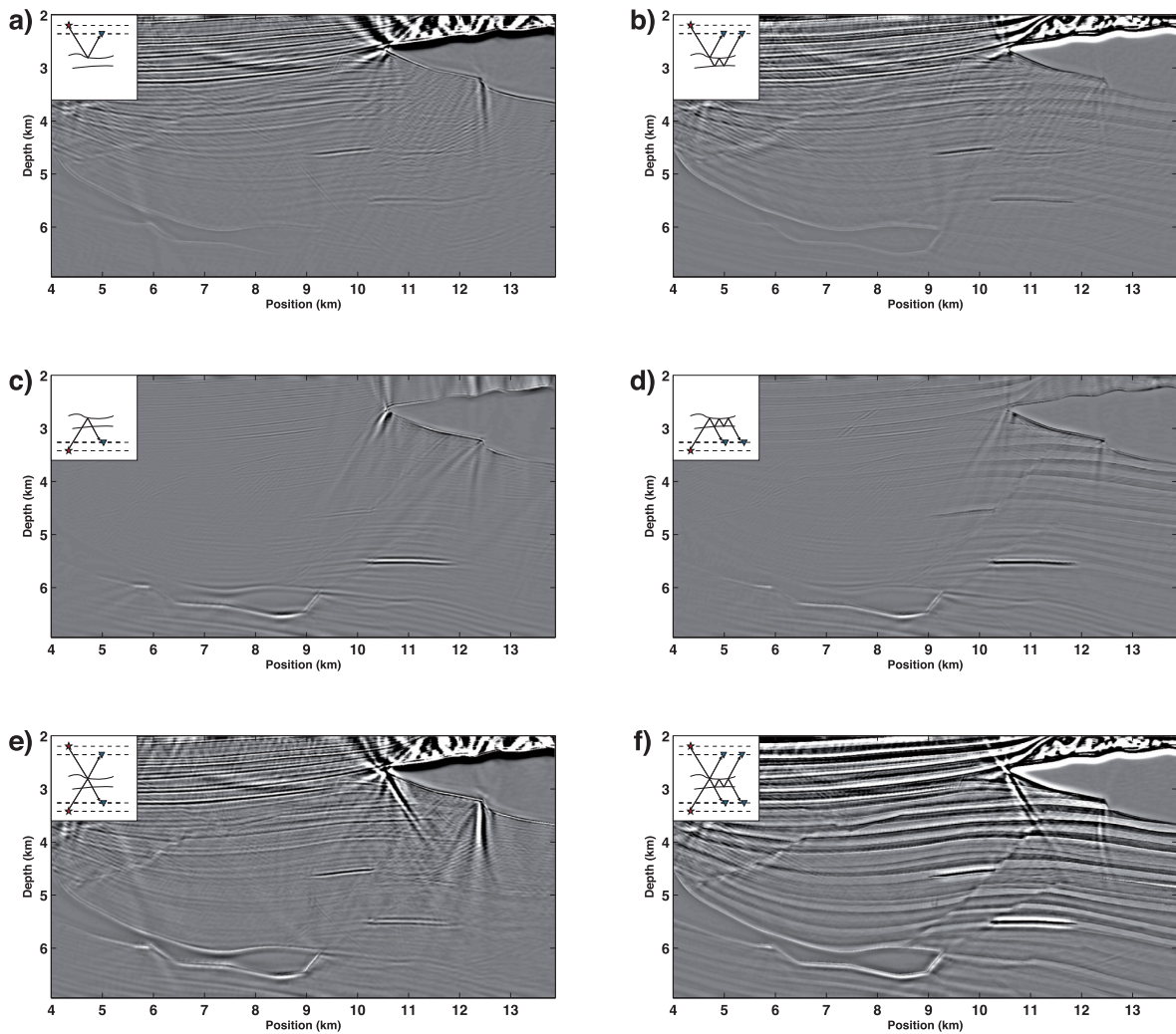


Figure 12. SS images for the six different imaging experiments depicted in Fig. 3.

Shen *et al.* 2011), and illumination weights can then be applied to the migrated gathers to correct these effects (Fletcher *et al.* 2012; Archer *et al.* 2013).

Despite the evident improvements when accounting for multiples and incomplete boundaries in the imaging process, fully enclosing boundaries and non-linear interactions are not explicitly required in the original formulation of the imaging problem which was based on the concepts of the so-called adjoint-state method (Baysal *et al.* 1983; Tarantola 1984). These requirements do become explicit under the SRI formalism (Halliday & Curtis 2010; Vasconcelos 2013; Ravasi & Curtis 2013b), which we use here to perform linear and non-linear ERTM: the contribution of high-order scattering interactions allows for power conservation in scattering (Fleury *et al.* 2010; Wapenaar *et al.* 2010; Douma *et al.* 2011), while that of complete boundaries guarantees the presence of both stationary points that bring physical energy and those that suppress non-physical arrivals (Meles & Curtis 2013; Loer *et al.* 2014).

It is worth pointing out that although our model design may not look entirely realistic, especially because of our choice to add a second water layer below the imaging target (definitely not the case for real field experiments), this does not preclude any of our observations about the increased illumination and artefact reduction given by sources (and receivers) below the imaging target. We conjecture that having P -wave only sources and a seabed acting as a P -to- S

wave converter might be an alternative (approximately equivalent) approach to that of having both P - and S -wave sources in a fully elastic layer at depth, and so similar results would be obtained if we were able to record (or more likely, reconstruct) these wavefields.

In our examples data from bottom boundaries of sources and receivers and full propagators required by eqs (3)–(5) are directly modelled and hence are exact. In practice, when only a reference (smooth) version of the velocity model is available, these fields cannot be modelled directly. In acoustic media, these wavefields can

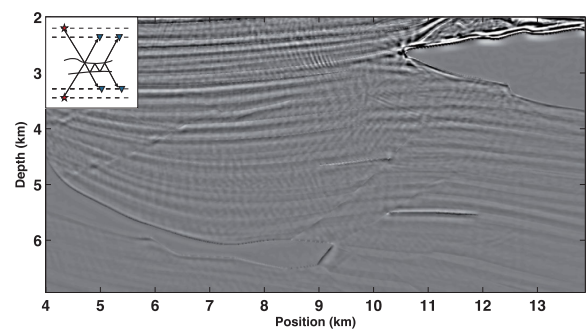


Figure 13. PS non-linear image using sources and receivers both above and below the imaging target without correction for polarity reversal.

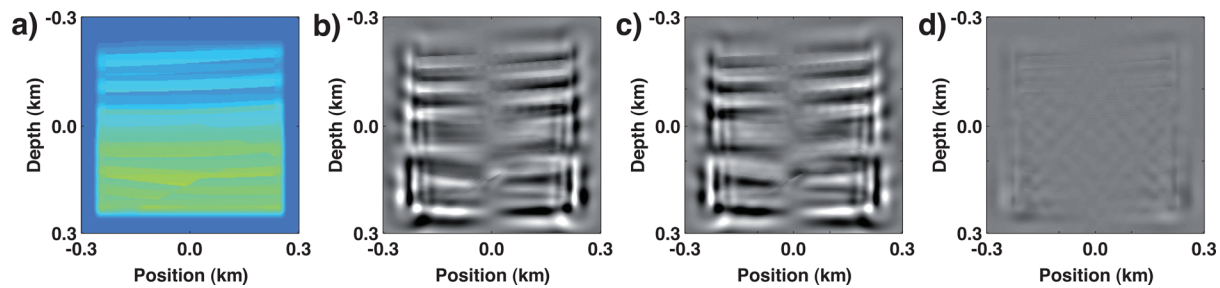


Figure 14. *PS* imaging using an enclosing boundary of sources of ray $r = 0.5$ km (a) *P*-wave velocity model. A portion of the Pluto model in Fig. 3(a) is extracted and embedded in an otherwise homogenous medium with $v_P = 2000$ m s⁻¹, $v_S = 1000$ m s⁻¹ and $\rho = 1000$ kg m⁻³. Shear wave properties are the same as those in the Pluto model used in the previous example. (a) Linear imaging as defined by eq. (6), (b) non-linear terms of the non-linear imaging eqs (3)–(5) and (c) ‘full’ non-linear imaging—the sum of the linear (a) and non-linear (b) terms.

be estimated by applying the ‘Marchenko redatuming’ approach of Broggini *et al.* (2012) and Wapenaar *et al.* (2013). This method constructs the full wavefield from a virtual source or receiver anywhere inside the medium (without needing a physical receiver or source at the location of interest), from one-sided reflection data and an estimate of the direct arriving wave-front from the virtual source to the recording surface. Whether the uplift in the image quality given by non-linear two-sided imaging will be similar to that observed in our examples depends on the accuracy of the reconstruction of these fields in complex geologies (van der Neut *et al.* 2014), and when only limited-aperture arrays of sources and receivers are available. Moreover, this approach has recently been developed also for electromagnetic media (Slob & Wapenaar 2013), and the first extension to elastic data is in da Costa *et al.* (2014).

5 CONCLUSION

In this paper, source–receiver interferometric imaging is used to create elastic images of the subsurface that represent the local interaction between *P* and *S* waves within the subsurface. *P*-to-*P*, *P*-to-*S* and *S*-to-*S* images are computed by means of linear (i.e. using only primary reflections) and non-linear (exploiting also multiple reflections) imaging, using one- and two-sided acquisition geometries.

Conventional elastic reverse-time migration produces images that exhibit acquisition imprints and poorly illuminated areas, especially for highly complex subsurface environments. Exploiting multiple reflections in the imaging process (using non-linear reverse-time migration) with the correct full or scattered source and receiver propagators mitigates these problems and increases the resolution of the migrated image because multiples provide better subsurface illumination. Imaging with two-sided acquisition geometries can also make use of the information contained in the transmitted component of the recorded wavefield which is shown to be beneficial, particularly for providing low wavenumber information.

When imaging with converted waves special attention must be given to the physical meaning of the resulting image: a ‘structural’ image can be obtained from *P*-to-*S* conversions by applying one of the several available polarity correction procedures to reduce the destructive interference in the stacked image. However, true-amplitude imaging has no meaning if the response at zero-time and zero-offset is sought, because this is null by the interferometry-based; since the image will not be zero in real acquisition scenarios due to their practical limitations, the amplitudes retrieved are due entirely to these limitations rather than to the subsurface properties. If used quantitatively, these amplitudes would tend to mislead subsequent geological interpretation. Other quantitative definitions of

P-to-*S* images are conceivable, however, those will require further research.

ACKNOWLEDGEMENTS

This work was performed while Matteo Ravasi was an intern at Schlumberger Gould Research. The authors thank Schlumberger for support and permission to publish this paper. Matteo Ravasi and Andrew Curtis are grateful to the other sponsors of the Edinburgh Interferometry Project (EIP) (ConocoPhillips, Statoil and Total). We are thankful to James Rickett and Dirk-Jan van Manen for insightful discussions and inputs. The comments of the editor Andrea Morelli, Kees Wapenaar, and an anonymous reviewer helped to improve this paper. We also acknowledge the SMAART JV consortium for releasing the Pluto 1.5 synthetic data set.

REFERENCES

- Amundsen, L., 2001. Elimination of free-surface related multiples without need of the source wavelet, *Geophysics*, **66**, 327–341.
- Archer, S., Du, X. & Fletcher, R., 2013. Amplitude inversion of depth-imaging seismic data from areas with complex geology, in *Proceedings of the 75th EAGE Conference & Exhibition*, London.
- Balch, A. & Erdemir, C., 1994. Sign-change correction for prestack migration of P-S converted wave reflections, *Geophys. Prospect.*, **42**, 637–663.
- Baysal, E., Kosloff, D. & Sherwood, J. Reverse time migration, *Geophysics*, **48**, 1514–1524.
- Berkhout, A.J. & Verschuur, D.J., 1997. Estimation of multiple scattering by iterative inversion; Part I: theoretical considerations, *Geophysics*, **62**, 1586–1595.
- Berkhout, A.J. & Verschuur, D.J., 2011. Full wavefield migration, utilizing surface and internal multiple scattering, in *Proceedings of the 81st Annual Meeting*, Las Vegas, SEG, Expanded Abstracts, pp. 3212–3216.
- Biondi, B., 2006, *3D Seismic Imaging*, SEG.
- Broggini, F., Snieder, R. & Wapenaar, K., 2012. Focusing the wavefield inside an unknown 1D medium—beyond seismic interferometry, *Geophysics*, **77**(5), A25–A28.
- Chang, W.-F. & McMechan, G.A., 1994. 3-D elastic prestack, reverse-time depth migration, *Geophysics*, **59**(4), 597–609.
- Claerbout, J.F., 1971. Toward a unified theory of reflector mapping, *Geophysics*, **36**(3), 467–481.
- Curtis, A., 2009. Source-receiver seismic interferometry, in *Proceedings of the 79th Annual Meeting*, Houston, SEG, Expanded Abstracts, pp. 3655–3659.
- Curtis, A. & Halliday, D., 2010. Source-receiver wave field interferometry, *Phys. Rev.*, **81**, 046601-1–046601-10.
- da Costa, C., Ravasi, M., Meles, G. & Curtis, A., 2014. Elastic autofocusing, in *Proceedings of the 76th EAGE Conference & Exhibition*, Amsterdam, Extended Abstracts.

- Davydenko, M. & Verschuur, D.J., 2012. Demonstration of full wavefield migration in 2D subsurface models, in *Proceedings of the 74th EAGE Conference & Exhibition*, Copenhagen.
- Denli, H. & Huang, L., 2008. Elastic-wave reverse-time migration with a wavefield separation imaging condition, in *Proceedings of the 78th Annual Meeting*, Las Vegas, SEG, Expanded Abstracts, pp. 2346–2350.
- Douma, H., Vasconcelos, I. & Snieder, R., 2011. The reciprocity theorem for the scattered field is the progenitor of the generalized optical theorem, *J. acoust. Soc. Am.*, **129**, 2765–2771.
- Du, Q., Zhu, Y. & Ba, J., 2012. Polarity reversal correction for elastic reverse time migration, *Geophysics*, **77**, S31–S41.
- Esmersoy, C. & Oristaglio, M., 1988. Reverse-time wave-field extrapolation, imaging, and inversion, *Geophysics*, **53**, 920–931.
- Fletcher, R., Archer, S., Nichols, D. & Mao, W., 2012. Inversion after depth imaging, in *Proceedings of the 82nd Annual International Meeting*, Houston, SEG, Expanded Abstracts, pp. 1–5.
- Fleury, C., 2013. Increasing illumination and sensitivity of reverse-time migration with internal multiples, *Geophys. Prospect.*, **61**(1), 891–906.
- Fleury, C., Snieder, R. & Larner, K., 2010. General representation theorem for perturbed media and application to green's function retrieval for scattering problems, *Geophys. J. Int.*, **183**, 1648–1662.
- Fleury, C. & Vasconcelos, I., 2012. Imaging condition for nonlinear scattering-based imaging: estimate of power loss in scattering, *Geophysics*, **77**(1), S1–S18.
- Gaiser, J. & Vasconcelos, I., 2010. Elastic interferometry for OBC data: theory and examples, *Geophys. Prospect.*, **58**(3), 347–360.
- Gardner, G.H.F., Gardner, L.W. & Gregory, A.R., 1974. Formation velocity and density—the diagnostic basics for stratigraphic traps, *Geophysics*, **39**, 770–780.
- Gherasim, M., Albertin, U., Nolte, B. & Askim, O., 2010. Wave-equation angle-based illumination weighting for optimized subsalt imaging, in *Proceedings of the 80th Annual International Meeting*, Denver, SEG, Expanded Abstracts.
- Halliday, D. & Curtis, A., 2010. An interferometric theory of source-receiver scattering and imaging, *Geophysics*, **75**, SA95–SA103.
- Jakubowicz, H., 1998. Wave equation prediction and removal of interbed multiples, in *Proceedings of the 68th Annual International Meeting*, New Orleans, SEG, Expanded Abstracts, pp. 1527–1530.
- Lecomte, I., 2008. Resolution and illumination analyses in PSDM: a ray-based approach, *Leading Edge*, **7**, 650–663.
- Liu, Y., Chang, X., Jin, D., He, R., Sun, H. & Zheng, Y., 2011. Reverse time migration of multiples for subsalt imaging, *Geophysics*, **76**(5), WB209–WB216.
- Loer, K., Meles, G., Curtis, A. & Vasconcelos, I., 2014. Diffracted and pseudo-physical waves from spatially-limited arrays using source-receiver interferometry (SRI), *Geophys. J. Int.*, **196**(2), 1043–1059.
- Meles, G.A. & Curtis, A., 2013. Physical and non-physical energy in scattered wave source-receiver interferometry, *J. acoust. Soc. Am.*, **133**(6), 3790–3801.
- Muijs, R., Robertsson, J.O.A. & Holliger, K., 2007. Prestack depth migration of primary and surface-related multiple reflections: part I—imaging, *Geophysics*, **72**(2), S59–S69.
- Nemeth, T., Chengjun, W. & Schuster, G.T., 1999. Least-squares migration of incomplete reflection data, *Geophysics*, **64**, 208–211.
- Oristaglio, M.L., 1989. An inverse-scattering formula that uses all the data, *Inverse Problems*, **5**, 1097–1105.
- Ravasi, M. & Curtis, A., 2013a. Nonlinear scattering based imaging in elastic media: theory, theorems and imaging conditions, *Geophysics*, **78**(3), S137–S155.
- Ravasi, M. & Curtis, A., 2013b. Elastic imaging with exact wavefield extrapolation for application to ocean bottom 4C seismic data, *Geophysics*, **78**(6), S265–S284.
- Rosales, D.A., Fomel, S., Biondi, B.L. & Sava, P., 2008. Wave-equation angle-domain common-image gathers for converted waves, *Geophysics*, **73**, S17–S26.
- Shen, H., Mothi, S. & Albertin, U., 2011. Improving subsalt imaging with illumination-based weighting of RTM 3D angle gathers, in *Proceedings of the 81st Annual International Meeting*, San Antonio, SEG, Expanded Abstracts.
- Slob, E. & Wapenaar, K., 2013. Coupled Marchenko equations for electromagnetic Green's function retrieval and imaging, in *Proceedings of the 83rd Annual International Meeting*, Houston, SEG, Expanded Abstracts.
- Stoughton, D., Stefani, J. & Michell, S., 2001. 2-D elastic model for wavefield investigations of subsalt objectives, deep water Gulf of Mexico, *Proceedings of the 71st Annual International Meeting*, San Antonio, SEG, Expanded Abstracts, pp. 1269–1272.
- Tarantola, A., 1984. Inversion of seismic reflection data in the acoustic approximation, *Geophysics*, **49**, 1259–1266.
- ten Kroode, F., 2002. Prediction of internal multiples, *Wave Motion*, **35**, 315–338.
- van der Neut, J., Almagro Vidal, C., Grobbe, N. & Wapenaar, K., 2013. Turning one-sided illumination into two-sided illumination by target-enclosing interferometric redatuming, in *Proceedings of the 75th EAGE Conference & Exhibition*, London.
- van der Neut, J., Vasconcelos, I. & Wapenaar, K., 2014. An interferometric interpretation of Marchenko redatuming, in *Proceedings of the 76th Annual EAGE Meeting*, Amsterdam.
- van Manen, D.-J., Curtis, A. & Robertsson, J.O.A., 2006. Interferometric modeling of wave propagation in inhomogeneous elastic media using time reversal and reciprocity, *Geophysics*, **71**, SI47–SI60.
- van Manen, D.-J., Robertsson, J.O.A. & Curtis, A., 2007. Exact wavefield simulation for finite-volume scattering problems, *J. acoust. Soc. Am.*, **122**(4), EL115–EL121.
- Vasconcelos, I., 2008. Generalized representations of perturbed fields—applications in seismic interferometry and imaging, in *Proceedings of the 77th Annual International Meeting*, Las Vegas, SEG, Expanded Abstracts, pp. 2927–2931.
- Vasconcelos, I., 2013. Source-receiver reverse-time imaging of dual-source, vector-acoustic seismic data, *Geophysics*, **78**(2), WA147–WA158.
- Vasconcelos, I., Snieder, R. & Hornby, B., 2008. Imaging internal multiples from subsalt VSP data Examples of target-oriented interferometry, *Geophysics*, **73**, S157–S168.
- Vasconcelos, I., Snieder, R. & Douma, H., 2009. Representation theorems and Green's function retrieval for scattering in acoustic media, *Phys. Rev. E*, **80**, 036605.
- Vasconcelos, I., Sava, P. & Douma, H., 2010. Nonlinear extended images via image-domain interferometry, *Geophysics*, **75**, SA105–SA115.
- Vasmel, M., Robertsson, J.O.A., van Manen, D.-J. & Curtis, A., 2013. Immersive experimentation in a wave propagation laboratory, *J. acoust. Soc. Am.*, **134**(6), EL492–EL498.
- Verschuur, D.J., Berkhout, A.J. & Wapenaar, C.P.A., 1992. Adaptive surface-related multiple elimination, *Geophysics*, **75**(9), 1166–1177.
- Wapenaar, K. & Fokkema, J., 2006. Green's function representations for seismic interferometry, *Geophysics*, **71**, SI33–SI46.
- Wapenaar, K., Slob, E. & Snieder, R., 2010. On seismic interferometry, the generalized optical theorem, and the scattering matrix of a point scatterer, *Geophysics*, **75**, SA27–SA35.
- Wapenaar, K., Broggini, F. & Snieder, R., 2012. Creating a virtual source inside a medium from reflection data: heuristic derivation and stationary-phase analysis, *Geophys. J. Int.*, **190**(2), 1020–1024.
- Wapenaar, K., Broggini, F., Slob, E. & Snieder, R., 2013. Three-dimensional single-sided Marchenko inverse scattering, data-driven focusing, Green's function retrieval, and their mutual relations, *Phys. Rev. Lett.*, **110**(8), 084301.
- Weglein, A., Gasparotto, F., Carvalho, P. & Stolt, R., 1997. An inverse-scattering series method for attenuating multiples in seismic reflection data, *Geophysics*, **62**, 1975–1989.
- Yan, J. & Sava, P., 2008. Isotropic angle-domain elastic reverse-time migration, *Geophysics*, **73**, S229–S239.
- Zhang, D. & Schuster, G.T., 2014. Least-square reverse time migration of multiples, *Geophysics*, **79**, S11–S21.